JGR Solid Earth

RESEARCH ARTICLE
10.1029/2019JB018517

Fault Reactivation During Fluid Pressure Oscillations: Transition From Stable to Unstable Slip

Corentin Noël[1], François X. Passelègue[1], Carolina Giorgetti[1], and Marie Violay[1]

[1]Laboratory of Experimental Rock Mechanics, Ecole Polytechnique Fédérale de Lausanne, Lausanne, Switzerland

Key Points:

- Laboratory investigation of the effect of fluid pressure oscillations on the fault stability behavior
- Fluid pressure signal controls the time distribution of the instabilities
- Fluid pressure oscillations promote seismic rather than aseismic slip; the higher the amplitude of the oscillations the more unstable the fault is

Correspondence to:
C. Noël,
corentin.noel@epfl.ch

Citation:
Noël, C., Passelègue, F. X., Giorgetti, C., & Violay, M. (2019). Fault Reactivation During Fluid Pressure Oscillations: Transition From Stable to Unstable Slip. *Journal of Geophysical Research: Solid Earth*, *124*, 10,940–10,953. https://doi.org/10.1029/2019JB018517

Received 8 AUG 2019
Accepted 18 OCT 2019
Published online 7 NOV 2019

Abstract High-pressure fluid injection in deep georeservoirs can induce earthquakes. Recent observations suggest that cyclic injections might trigger less seismicity than monotonic injections. Here, we report triaxial laboratory experiments conducted on faulted quartz-rich sandstone that provide new insight into the physics of fault-fluid interactions subjected to cyclic fluid pressure variations. The experiments were performed at 30 and 45 MPa confining pressure, imposing constant or sinusoidal fluid pressure oscillations of amplitudes ranging from 0 to 8 MPa in addition to a far-field constant loading rate (10^{-4} and 10^{-3} mm s^{-1}). The results show that (i) in agreement with the Mohr-Coulomb theory, faults reactivate at the static friction criterion, which is generally reached at the maximum fluid pressure during oscillations. (ii) Oscillating fluid pressure perturbations promote seismic behavior rather than aseismic slip, and (iii) increasing the oscillation's amplitude enhances the onset of seismic activity along the fault. We demonstrate that this behavior is caused by slip rate variations resulting from the fluid pressure oscillations. Without fluid pressure oscillations, increasing the far-field loading rate also promotes seismic activity. Our experiments demonstrate that the seismicity intensification due to cyclic fluid injections could be promoted at shallow depth, where confining pressure is relatively low, resulting in large strain rate perturbations.

1. Introduction

In the past 20 years, the growing interest in and the use of deep georeservoirs for purposes such as carbon storage, waste water disposal, or geothermal energy exploitation has induced massive increases in seismicity in some normally "quiet" regions (e.g., Ellsworth, 2013). Indeed, high-pressure fluid injection can reduce the effective normal stress ($\sigma_n - P_f$) acting on a fault, bringing the system closer to failure. If the effect of a linear increase in fluid pressure on fault reactivation has been widely studied (e.g., French et al., 2016; Passelègue et al., 2018; Rutqvist et al., 2016; Scuderi & Collettini, 2018), only little is known about cyclic fluid pressure perturbations (Chanard et al., 2019; Farquharson et al., 2016; Noël et al., 2019). In addition, while the quasi-static reactivation of faults is well understood, the influence of such fluid pressure perturbations on the slip behavior of faults remains poorly constrained. Yet, such fluid pressure perturbations are common in the upper crust. They can originate from natural causes such as oceanic tides (e.g., Wang & Davis, 1996), seasonal hydrology (e.g., Bettinelli et al., 2008; Chanard et al., 2014), gas-rich magma ascent in volcanic edifices (e.g., Michaut et al., 2013), or originate from anthropogenic causes due to fluid production from (e.g., Candela et al., 2019) or injection into georeservoirs (e.g., Verdon et al., 2013).

Based on anthropogenic perturbation, it has been suggested that cyclic fluid stimulation results in a different seismic response of the reservoir compared to monotonic fluid injections. Cyclic injections seem to trigger less induced seismicity than traditional monotonic injections (Yoon et al., 2014; Zang et al., 2013). Recent in situ and laboratory studies experimented with cyclic injection strategies and found that not only the number of seismic events but also the maximum recorded event magnitude are reduced (Zang et al., 2018). With the growing interest in the use of georeservoirs, such cyclic stimulation might be of great interest for future injections. However, only a small number of experimental studies have been performed with the aim of increasing the comprehension of such phenomena, and those were mainly conducted on intact rock samples (Chanard et al., 2019; Farquharson et al., 2016; Noël et al., 2019; Zhuang et al., 2016).

In this paper, we report triaxial deformation experiments performed on faulted Fontainebleau sandstone (FS), a quartz-rich sandstone. Particularly, we focus on the effect of oscillating fluid pressure.

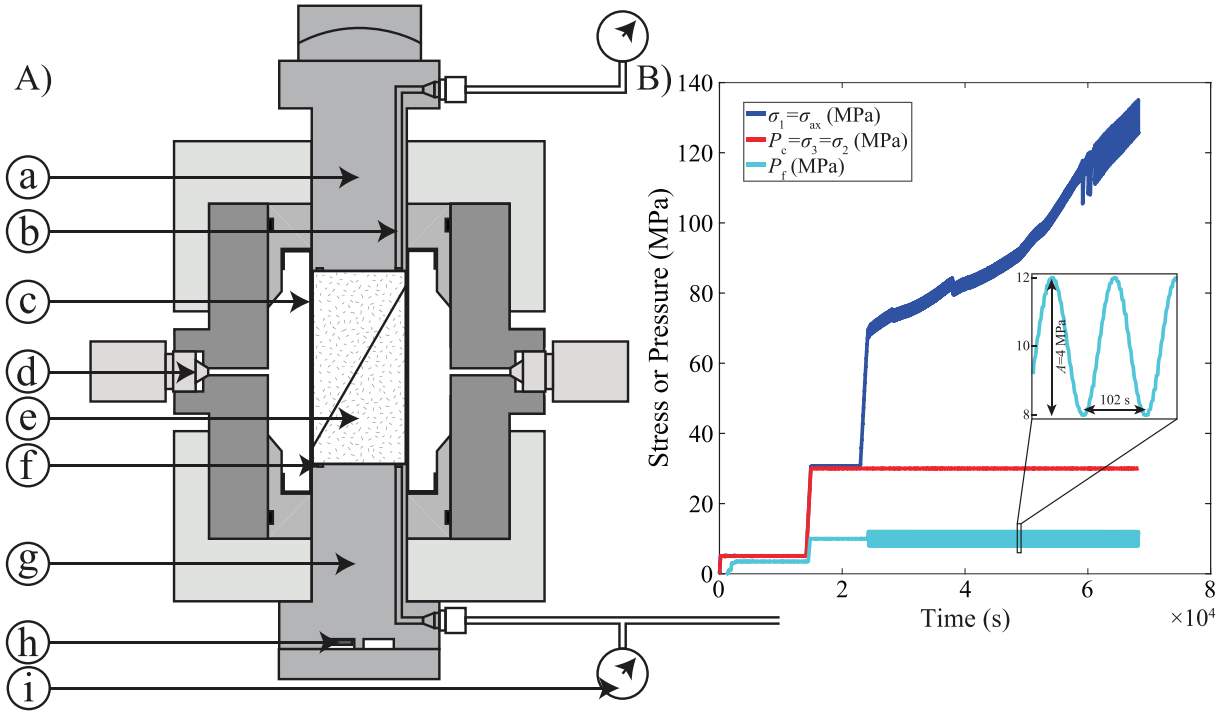

Figure 1. (a) Cross-section drawing of the Hoek cell used for triaxial experiments. (a) top piston, (b) fluid pipes, (c) jacket, (d) confining oil inlet, (e) saw-cut sample, (f) drainage groves allowing homogeneous fluid pressure distribution, (g) bottom piston, (h) acoustic emission sensor, and (i) pressure sensor. (b) Axial stress, confining, and fluid pressure applied as function of time. The inset displays the fluid pressure oscillations imposed during the experiment.

2. Experimental Methodology

2.1. Starting Sample

FS (south of Paris, France) was used as starting material for this study. It is composed of almost 100% quartz, with randomly oriented grains cemented by quartz. The connected porosity was measured to be 6.5% ± 0.3% at ambient conditions using the triple weight method (see Guéguen & Palciauskas, 1994). The permeability was measured using the steady-state Darcy flow method. Increasing the effective confining pressure from 20 to 50 MPa leads to a decrease of the permeability from 4 to 2×10^{-15} m^2. Cylinders of FS were diamond drilled (36.5-mm diameter), sawed, and opposite faces ground flat to prevent any parallelism defects (±100 μm precision). Cylinders were then sawed at $\alpha = 30°$ from their axes to create an elliptical fault interface. The fault surfaces were rectified and then polished with a Struers® MDpiano 80 abrasive disk (comparable to no. 80 SiC abrasive paper). The roughness of each fault surface was measured on a 1 × 1-cm area using a 3-D optical profilometer (Contour GT-I 3D-Optical Microscope, Bruker). The initial roughness (here, defined as the mean quadratic height of the surface [Rq]) before sample deformation was mainly controlled by the porosity and was found to be characterized by Rq = 17.4 ± 0.5 μm. According to the permeability (k), the sample length ($l = 75$ mm), water viscosity ($\eta = 10^{-3}$ Pa s), and typical storage capacity ($\beta = 10^{-11}$ Pa^{-1}) values for FS (Duda & Renner, 2013; Song & Renner, 2008), the characteristic time for water to diffuse across the sample was computed via $t_d = \frac{l^2\eta\beta}{k}$ (Fischer & Paterson, 1989). We found $t_d < 1$ s, and we planned our experiments so that the samples were always macroscopically drained, that is, t_d << oscillations period.

2.2. Apparatus

We used an instrumented Hoek cell (Figure 1a) placed under a uniaxial press (Walter and Bai) as the deforming apparatus. The system allowed for an oil confining pressure ($P_c = \sigma_2 = \sigma_3$) up to 70 MPa (±50-kPa resolution) and a maximum axial stress ($\sigma_{ax} = \sigma_1$) of 1 GPa (±100-kPa resolution). Fluid pressure (de-aired distilled water, P_f) was imposed from the bottom of the sample with a step motor pump. The pore fluid pump had a 200-cm^3 capacity and allowed for pressures up to 15 MPa. P_f was measured at the top and the bottom of the sample using precision pressure sensors (±10-kPa resolution). Pump fluid volume (V_f) variation was also

monitored thanks to encoders directly mounted on the pump (±1-mm^3 resolution). In addition, piezoceramic crystal (PI ceramic PRYY + 0400, 5-mm diameter and 1 mm thick) was glued to the bottom piston to monitor high-frequency acoustic emission (AE) events radiated from the samples during the tests. The emitted signal was amplified to 40 dB through a preamplifier. The trigger was set to only record events with an amplitude higher than 0.056 V, that is, ≈1.75 times higher than the background noise of the experimental setup (measured at 0.032 V) to prevent noise recording. Each event that fulfilled this criterion was recorded at a 1-MHz sampling rate, within a time window of 400 μs. Axial displacements were measured using linear optoelectronic transducers mounted outside of the cell with a precision of 1 μm. The contribution of the jacket during the sample deformation was evaluated by shearing a faulted aluminum sample (precut at 30° from its axis), having its opposite faces covered with a Teflon sheet. The jacket contribution was found to be negligible under the tested stress conditions.

2.3. Experimental Procedure

The procedure applied is presented in Figure 1b. Faulted FS samples were placed into the Hoek cell and P_c was increased to 5 MPa. The sample was then pumped down to vacuum and pore fluid was injected at 1 MPa from the bottom piston. Once fluid pressure was equilibrated at the bottom and the top of the sample, P_f was increased to 3 MPa (i.e., $P_c - P_f = 2$ MPa) for 5 to 8 hr to ensure full sample saturation. Then, confining and fluid pressure were increased together to $P_c = 30$ or 45 MPa and $P_f = 10$ MPa. When V_f was equilibrated, the axial stress was increased by applying a constant and slow far-field loading rate (v_{ax}, between 10^{-4} and 10^{-3} mm s^{-1}) on the axial pistons. Experiments were performed either with constant or cyclic (sinusoidal) fluid pressure. For cyclic fluid pressure experiments, the oscillations started only once the sample started to behave inelastically (stress-displacement curve deviating from linearity). The oscillations were imposed around a mean value of $P_f^{mean} = 10$ MPa with a peak-to-peak amplitude (A) ranging from 1 to 8 MPa and a constant period of 102 s, systematically allowing the sample to remain under macroscopic drained conditions.

2.4. Data Analysis

Friction along the fault interface (μ) was computed as the ratio between the shear stress (τ) and the effective normal stress ($\sigma_n - P_f$), calculated from the principal stress following

$$\mu = \frac{\tau}{\sigma_n - P_f}, \tag{1a}$$

with

$$\tau = \frac{\sigma_1 - \sigma_3}{2} \sin(2\alpha), \tag{1b}$$

and

$$\sigma_n = \frac{\sigma_1 + \sigma_3 - 2P_f}{2} - \frac{\sigma_1 - \sigma_3}{2} \cos(2\alpha), \tag{1c}$$

where σ_1 and σ_3 are the axial and the radial stresses, respectively, and α is the angle between the axial stress and the fault plane.

For the experiments where fluid pressure oscillated, we investigated the correlation between fast audible stress drops (hereafter referred to as stick-slip or unstable slip) and AE events with the fluid pressure oscillations. First, for each experiment, stick-slip and AE events were split with time intervals corresponding to the period of the fluid pressure oscillation as described in Noël et al. (2019). This allowed for the estimation of the distribution of events over the period of a fluid pressure oscillation. Second, to further investigate the correlation between the events and fluid pressure oscillations, AE events catalog was treated following Schuster's method (Schuster, 1897). In the events catalog, each event was attributed a phase angle and a unit length that depends on its position with respect to a forcing function (here the fluid pressure oscillations). Thus, each event was represented by a phasor of unit length. The sum of the N event phasors gave a vector of length R. The probability of a random walkout to reach a distance R from the origin can be given by prob = $\exp(-R^2/N)$ (Heaton, 1975; Rydelek & Hass, 1994; Schuster, 1897). If the walkout exceeds a given

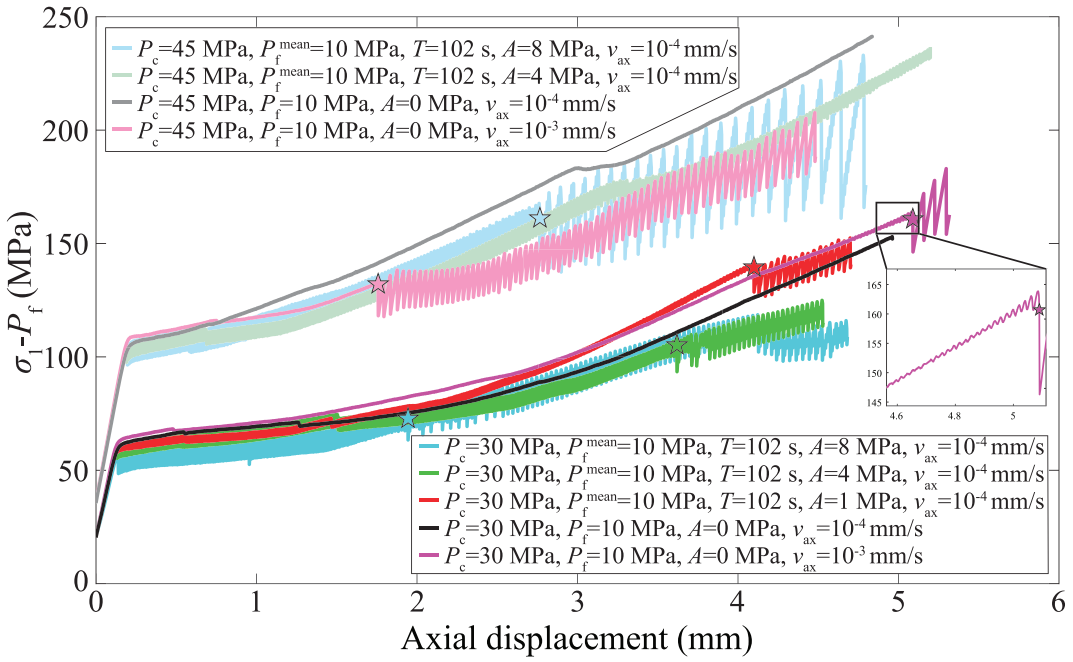

Figure 2. Effective axial stress as a function of axial displacement during triaxial deformation experiments. The insert window presents the transition from stable to unstable slip behavior during the experiment performed at P_c = 30 MPa and v_{ax} = 10^{-3} mm s^{-1}. If unstable behavior was observed during the experiment, the star indicates the onset of stick-slip motions.

length, then the probability that the event phases are nonrandom is high, and the catalog contains a significant correlation with the tested function. In our analysis, the fluid pressure maximum and minimum corresponded to a phase of 90° (i.e., upward) and 270° (i.e., downward), respectively.

3. Results

Stress-displacement curves (Figure 2) first show a linear increase of the effective axial stress ($\sigma_1 - P_f$) as the axial displacement increases (i.e., elastic behavior). This first elastic stage is followed by a deviation from linearity (i.e., onset of fault sliding) that occurs at $\mu \approx 0.53 \pm 0.02$, independent of the conditions tested. After this point, a stress hardening phase is observed, during which the fault slides in a stable manner. Finally, depending on the experimental conditions, the sliding behavior may become seismic.

For experiments performed at a slow loading rate (i.e., $v_{ax} = 10^{-4}$ mm s^{-1}), fluid pressure oscillations impact the slip behavior of the faulted sample. Indeed, when no oscillations are imposed, the fault always slides in a stable manner (black curve in Figure 2). However, when fluid pressure oscillations are imposed during the hardening stage, the fault first slides in a stable manner up to a point where a fast audible stress drop (i.e., unstable slip) occurs. Following the first unstable slip (denoted by a star in Figure 2), fault slip is mostly accommodated by a stick-slip sequence (i.e., repetitive unstable slip followed by nonsliding period during which the system primarily behaves elastically). The recorded stress drops during seismic events increase with the confining pressure (from 10 MPa when P_c = 30 MPa to about 20 to 40 when P_c = 45 MPa). Importantly, we observe that the transition from stable sliding to stick-slip depends on the fluid pressure oscillation amplitude. Increasing the amplitude of P_f advances the onset of unstable slip (Figure 2 and Table 1). Both the axial displacement (d_{ax}) and the effective axial stress ($\sigma_1 - P_f$) at the onset of stick-slips are reduced as the amplitude of P_f increases. For example, at P_c = 30 MPa, increasing the amplitude of P_f from 1 to 8 MPa advances the onset of unstable slip from d_{ax} = 4.1 to 1.9 mm and from $\sigma_1 - P_f$ = 139 to 72 MPa.

Without fluid pressure oscillations, experiments show that the loading rate (v_{ax}) also has an effect on the sliding behavior of the fault: At low v_{ax} (10^{-4} mm s^{-1}), the fault slip is always stable, whereas at higher v_{ax}

Table 1
Summary of the Triaxial Experiments Performed on Fontainebleau Sandstone Faulted Samples

		Fluid pressure		Loading rate	Onset of stick-slips		Max slip rate before stick-slip
	P_c	Mean	Amplitude	v_{ax}	d_{ax}	$\sigma_1 - P_f$	$\dot{\delta}_{max}$
Sample	(MPa)	(MPa)	(MPa)	(mm s^{-1})	(mm)	(MPa)	(mm s^{-1})
FSB24	30	10	-	10^{-3}	5.089	160.7	1.17×10^{-3}
FSB14	30	10	-	10^{-4}	-	-	1.43×10^{-4}
FSB16	30	10	1	10^{-4}	4.100	139.5	2.97×10^{-4}
FSB17	30	10	4	10^{-4}	3.620	150.2	6.06×10^{-4}
FSB12	30	10	8	10^{-4}	1.944	72.82	6.49×10^{-4}
FSB23	45	10	-	10^{-3}	1.758	132.1	1.17×10^{-3}
FSB18	45	10	-	10^{-4}	-	-	1.43×10^{-4}
FSB22	45	10	4	10^{-4}	-	-	6.41×10^{-4}
FSB19	45	10	8	10^{-4}	2.766	161.2	7.72×10^{-4}

(10^{-3} mm s^{-1}), a transition between stable sliding to stick-slip can be observed. At higher P_c, the transition occurs for shorter cumulative displacement than at lower P_c. This transition from stable to unstable behavior can be abrupt and unpredictable (e.g., for the experiment at $P_c = 45$ MPa) or more gentle with periodic slow stress release presenting stronger and stronger amplitude with increasing cumulative slip before the first stick-slip occurs (e.g., for the experiment at $P_c = 30$ MPa, see zoom in Figure 2).

Seismic correlations for experiments performed at $v_{ax} = 10^{-4}$ mm s^{-1}, $P_c = 30$ and 45 MPa are presented in Figure 3 and Figure 4, respectively. When $A = 0$ MPa, AE events are spread, and the random walks show no significant correlation with time. However, when $A > 0$ MPa, stick-slip events are triggered when the fluid pressure is close to its maximum, and an increase of AE events is concomitant with the maximum value of P_f. Increasing A tends to promote the occurrence of stick-slip and AE events around the peak of the P_f oscillations.

The random walks of experiments with $A > 0$ MPa (Figure 3 and Figure 4) show that AE events are highly correlated with the pore fluid oscillations (probability $\gg 99\%$). The phase correlation (i.e., phase at the end of the random walk, ψ) occurs either just at the peak of P_f (e.g., the experiment at $P_c = 30$ MPa and $A = 1$ MPa or the experiment at $P_c = 45$ MPa and $A = 8$ MPa with $\psi = 93°$ and 87°, respectively) or just before the peak of P_f (e.g., the experiment at $P_c = 30$ MPa and $A = 4$ MPa or the experiment at $P_c = 45$ MPa and $A = 4$ MPa with $\psi = 69°$ and 76°, respectively). For the experiment at $P_c = 30$ MPa and $A = 8$ MPa, the random walk shows two trends. First, AE events are mainly correlated with the maximum value of P_f ($\psi \approx 100°$), then they correlate with the maximum decreasing rate of P_f ($\psi \approx 180°$), and finally back with the maximum value of P_f ($\psi \approx 90°$).

4. Interpretation and Discussion

Our experimental results highlight that (i) stick-slip events are triggered after a certain amount of stable sliding that induces fault hardening. (ii) At a constant v_{ax}, fluid pressure oscillations promote unstable slip (i.e., stick-slips are triggered after a smaller displacement and at lower stresses). (iii) Increasing the amplitude of the oscillations advances the onset of unstable motion. (iv) When fluid pressure oscillations are imposed, instabilities (i.e., stick-slip and AE events) are mainly triggered close to the maximum value of fluid pressure.

In the following, we first give a brief overview of fault reactivation and frictional sliding stability conditions and then interpret and discuss our main observations.

4.1. Theoretical Framework for Fault Reactivation and Frictional Stability

Fault reactivation and fault stability can be described with two distinct criteria. On the one hand, the Mohr-Coulomb failure criterion describes the amount of shear stress (τ) required at a given normal stress (σ_n) to induce the onset of slip. It defines the shear strength of the fault and predicts its reactivation when $\tau \geq \mu(\sigma_n - P_f)$. On the other hand, the rate-and-state friction formulation provides a comprehensive analysis of the behavior once the fault slip has initiated. In this framework, the frictional response of a fault varies

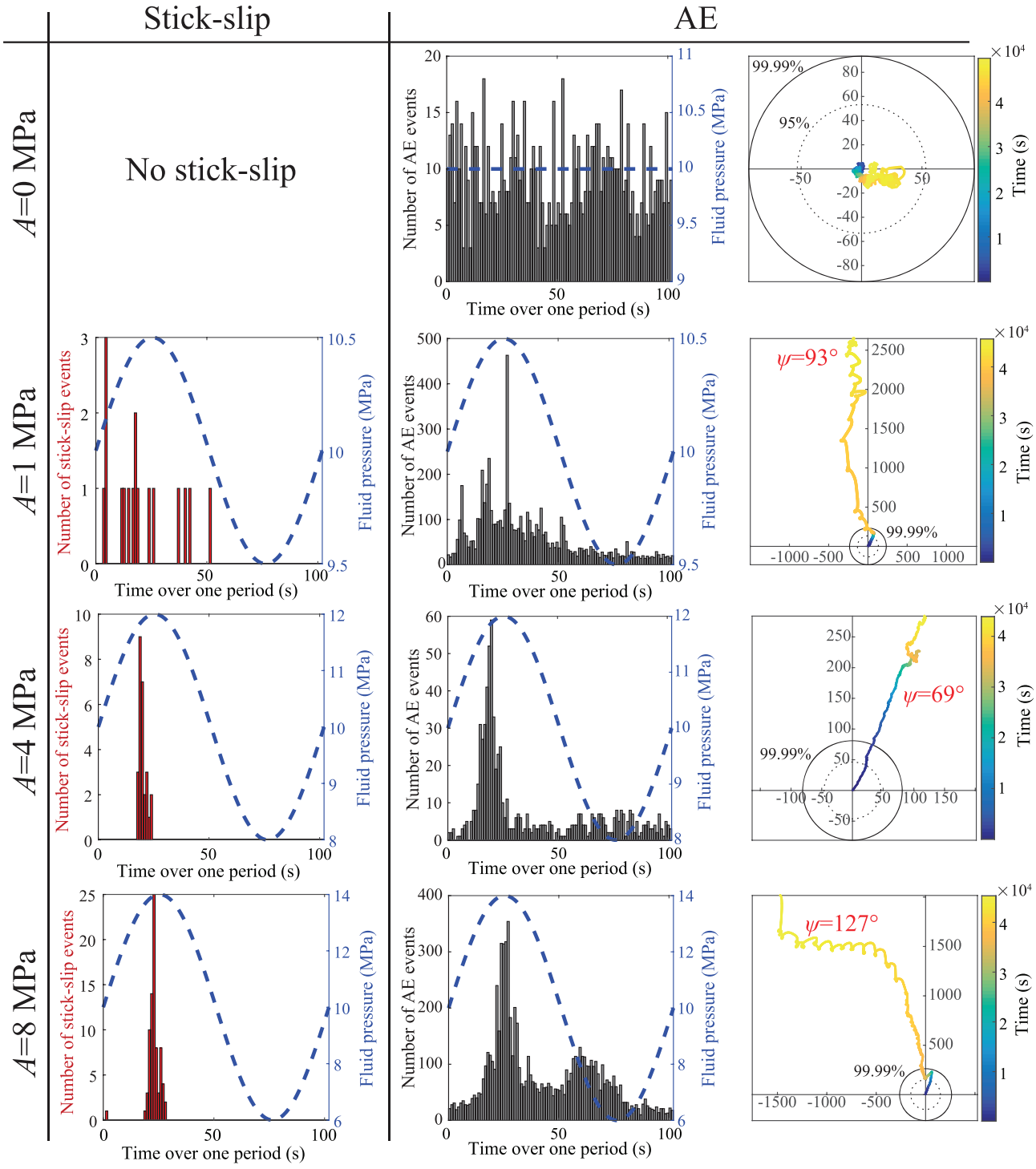

Figure 3. Event analyses for experiments performed at $P_c = 30$ MPa and $v_{ax} = 10^{-4}$ mm s^{-1} with various amplitudes of fluid pressure oscillations. Stick-slip events and acoustic emission (AE) events stacked over one oscillation period are displayed by red and gray bar charts, respectively. The bar charts represent the number of events, and the blue dashed lines represent the fluid pressure oscillations. A random walk of the catalog of AE events, with the experimental time shown by the color bar, is also presented. If the random walk exceeds a critical distance and has a high probability (>95%) of being correlated with the P_f oscillations, the phase at the end of the random walk (ψ) is noted. The maximum and minimum of fluid pressure correspond to a phase of 90° (i.e., upward) and 270° (i.e., downward), respectively. The probability distances 95% and 99.99% are plotted (dashed and full circle, respectively).

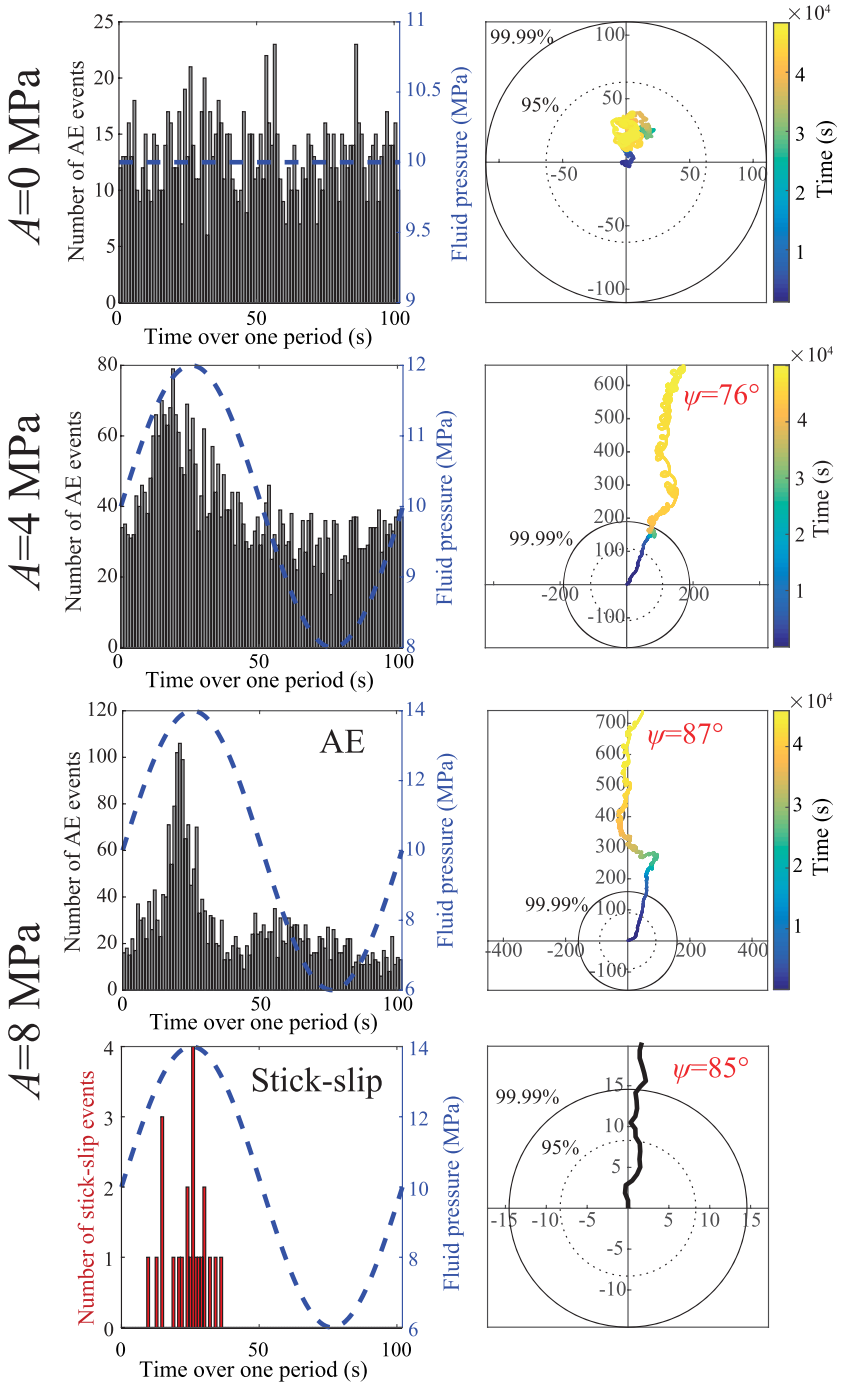

Figure 4. Event analyses for experiments performed at $P_c = 45$ MPa and $v_{ax} = 10^{-4}$ mm s^{-1} with various amplitudes of fluid pressure oscillations. Stick-slip events and acoustic emission (AE) events stacked over one oscillation period are displayed by red and gray bar charts, respectively. Stick-slip events occurred only for $A = 8$ MPa. The bar charts represent the number of events, and the blue dashed lines represent the fluid pressure oscillations. A random walk of the catalog of AE, with the experimental time shown by the color bar, and stick-slip events is also presented. If the random walk exceeds a critical distance and has a high probability (>95%) of being correlated with the P_f oscillations, the phase at the end of the random walk (ψ) is noted. The maximum and minimum of fluid pressure correspond to a phase of 90° (i.e. upward) and 270° (i.e., downward), respectively. The probability distances 95% and 99.99% are plotted (dashed and full circle, respectively).

with the loading history and depends on both the instantaneous slip rate and a state variable that describes the gradual evolution of the sliding interfaces (Dieterich, 1978; Ruina, 1983). Assuming these variables, the evolution of the frictional coefficient during slip can be estimated as follows:

$$\mu = \mu_0 + a\ln\left(\frac{V}{V_0}\right) + b\ln\left(\frac{V_0\theta}{D_c}\right), \tag{2a}$$

where, considering the so-called slip law, the state variable θ evolution is expressed as

$$\frac{d\theta}{dt} = -\frac{V\theta}{D_c}\ln\left(\frac{V\theta}{D_c}\right), \tag{2b}$$

with μ_0 being the reference friction at the velocity V_0, V the slip velocity, and D_c the critical slip distance. If the friction decreases as the sliding velocity increases (i.e., velocity weakening, $(a-b)<0$), the fault might experience dynamic instability; on the contrary, if the friction increases with an increasing sliding velocity (i.e., velocity strengthening, $(a-b)>0$), slip is accommodated by stable sliding.

Finally, when combined with the elastic dislocation theory (elliptical crack embedded in an isotropic elastic medium), the rate-and-state formulation states that if the stiffness of the elastic medium (K) is smaller than the critical fault stiffness (K_c), frictional instability can occur (e.g., Kanamori & Brodsky, 2004). Coupling the rate-and-state friction approach with a one-dimensional spring-slider model, the transition from stable to unstable slip can be found at the critical stiffness (Dieterich, 1979; Gu et al., 1984; Rice, 1993; Ruina, 1983):

$$K_c = \frac{(b-a)(\sigma_n - P_f)}{D_c}. \tag{3}$$

In summary, after fault reactivation (i.e., fault strength is overcome), the fault frictional behavior can be divided into three stability domains: (1) if $(a-b)>0$, the system is stable; (2) if $(a-b)<0$ and $K>K_c$, the system is conditionally stable (i.e., stable under quasistatic loading); or (3) if $(a-b)<0$ and $K<K_c$, the system is unstable.

Here we are interested in the effect of fluid pressure oscillations on the fault reactivation and stability. Using these theoretical formulations and considering drained and homogeneous conditions, a fluid pressure increase on the fault plane has two effects: First, it decreases the effective normal stress acting on the fault, promoting fault reactivation. Second, it can decrease the critical stiffness K_c, thus favoring slow and stable sliding rather than unstable events (i.e., earthquakes).

4.2. Fluid Pressure Oscillations Influences the Events Distribution

In agreement with Byerlee's rule (Byerlee, 1978), in the performed experiments, we observe a deviation from the elastic domain at $\mu \approx 0.53 \pm 0.02$. Moreover, when fluid pressure oscillations are imposed, instabilities (i.e., stick-slip and AE events) are being triggered close to the maximum value of fluid pressure. Increasing the amplitude of P_f accentuates this behavior (Figure 3 and Figure 4). Assuming a Coulomb failure criterion, a P_f increase has the effect of bringing the fault closer to failure independent of the fault slip behavior (stable or unstable). During the oscillating fluid pressure experiments, two parameters determine the moment when the fault strength will be reached: the increase in σ_1 and the oscillations imposed in P_f. Thus, a competition between the increase in σ_1 and the increase in P_f is occurring, that is, between v_{ax} (which affects σ_1) and the period of the P_f oscillations. Let us imagine that the period of P_f oscillation is infinitely long (or that v_{ax} is infinitely fast), in this case, the strength of the fault would be reached mainly due to the increase of σ_1 and P_f would have only a minor effect. On the contrary, if the period of the P_f oscillations is small compared to the increase in σ_1, the strength of the fault would be reached primarily due to the increase of P_f. Here, within one period of oscillation, the increase in σ_1 is low compared to the pore fluid variation such that stick-slip and AE events mainly occur around the maximum value of P_f. Increasing the amplitude from 1 to 8 MPa and keeping the same period of the oscillations amplifies this phenomenon as the strength of the fault is reached faster. In summary, the time distribution of the AE and stick-slip events is controlled by the Mohr-Coulomb failure criterion and depends on both the far-field loading and the period of the fluid pressure oscillations.

4.3. Fluid Pressure Oscillations Promoted Early Instability

In the performed experiments, stick-slips (i.e., unstable slip) are triggered after a long phase of stable sliding, sometimes preceded by smooth, slow stress release (Figure 2). The experiments show also that, at low v_{ax},

imposing fluid pressure oscillations facilitates unstable behavior (stick-slip). The higher the amplitude of the oscillations, the earlier stick-slip events are triggered. This transition can be explained by the fact that, even if the fault is velocity weakening (i.e., $(a - b) < 0$), the fault critical stiffness K_c is not reached from the beginning of the fault's sliding.

During our experiments, K_c depends on three parameters: (1) the slip hardening behavior, (2) the fluid pressure oscillations, and (3) the cumulative slip, such that

1. Due to the experimental configuration, while slip hardening occurs and the axial stress increases, the normal stress acting on the fault plane is also increasing. Increasing the effective normal stress acting on the fault increases K_c, moving the system toward unstable behavior (equation 3). Similar observations were made on quartz gouge where increasing the applied effective normal stress moved the system toward more unstable behavior (e.g., Leeman et al., 2018, 2016; Scuderi et al., 2017).
2. Fluid pressure oscillations also cause variation in the effective normal stress acting on the fault plane, thus provoking K_c oscillation.
3. The parameters a, b, and D_c may also change with the normal stress, slip rate, and accumulated displacement, which, in turn, may change the stability behavior of the system (e.g., Leeman et al., 2018; Mair & Marone, 1999; Marone & Scholz, 1988; Scuderi et al., 2017). Indeed, during the fluid pressure oscillation experiments, when looking at the slip rate along the fault as a function of time, we observe that increasing the amplitude of the oscillations affects the slip rate on the fault; the slip rate is oscillating in phase with the fluid pressure oscillations, and the maximum slip rate acting on the fault ($\dot{\delta}_{\max}$) is concomitant with the maximum value of P_f. $\dot{\delta}_{\max}$ increases from 1.43×10^{-4} to 6.49×10^{-4} mm s^{-1} increasing A from 0 to 8 MPa (Table 1). Moreover, without fluid pressure oscillations, increasing v_{ax} to 10^{-3} mm s^{-1} also facilitates stick-slip triggering (Figure 2).

The difference in the onset of unstable slip must originate from the fluid pressure oscillations. Indeed, for all the experiments, the hardening rate is similar (Figure 2) and cannot explain the enhancement of stick-slip events with increasing the amplitude of fluid pressure oscillation.

To test the other two hypotheses, we conducted complementary experiments that explored the influence of the normal stress of the fluid pressure and of the slip rate on the frictional properties of the experimental faults. These experiments consist of velocity step experiments, typically used to constrain the rate-and-state parameters (a, b, and D_c) of fault interfaces. These experiments were performed using the same apparatus and sample configuration described earlier. After saturation at low confining pressure, the samples were loaded to $P_c = 45$ MPa. Axial stress was increased by applying a constant loading rate while the normal stress was kept constant on the sample fault by regulating the confining pressure with a servo-controlled loop. The samples were first sheared at $v_{ax} = 10^{-3}$ mm s^{-1} for $d_{ax} = 1$ mm. Then, they were subjected to a sequence of increasing and decreasing v_{ax} between 10^{-5} and 3×10^{-3} mm s^{-1}, that is between 1.15×10^{-5} and 3.46×10^{-3} mm s^{-1} along the fault plane, for $d_{ax} = 0.1$ mm (Figure 5a). Two experiments were performed at $\sigma_n = 45$ MPa and at $P_f = 1$ and 10 MPa (i.e., two different effective normal stresses). This normal stress was chosen because it corresponds to the middle range of the normal stress applied during the experiments performed at $P_c = 30$ MPa. Then, we inverted the frictional parameters from experimental measurements by modeling the velocity steps, assuming the rate-and-state slip law (Ruina, 1983; equation 2). The inversion of the experimental data was made using the software package developed by Skarbek and Savage (2019; Figure 5b). The rate-and-state parameters found (Figure 6) show (i) No significant difference between the experiment with $P_f = 1$ or 10 MPa. (ii) A transition from positive to negative $(a - b)$ as the slip rate increased. The transition occurs around a velocity of 2×10^{-4} mm s^{-1} along the fault. (iii) D_c values do not show a significant variation with the slip rate or the effective normal stress. In summary, these results suggest that variations in the slip rate rather than in the effective normal stress are expected to promote the transition from stable to unstable slip.

Stability transitions with increasing loading rate have already been reported on granite (e.g., Kato et al., 1992; Mclaskey & Yamashita, 2017), metagabbro (e.g., Xu et al., 2018), and polycarbonate (e.g., Guérin-Marthe et al., 2019) dry meter-scale faulted samples. The transition is often attributed to a shrinking of the measured critical nucleation length (L_c) when increasing the loading rate. L_c is defined as the critical size that a sliding patch has to expand to become unstable and is inversely proportional to the critical stiffness K_c. In our

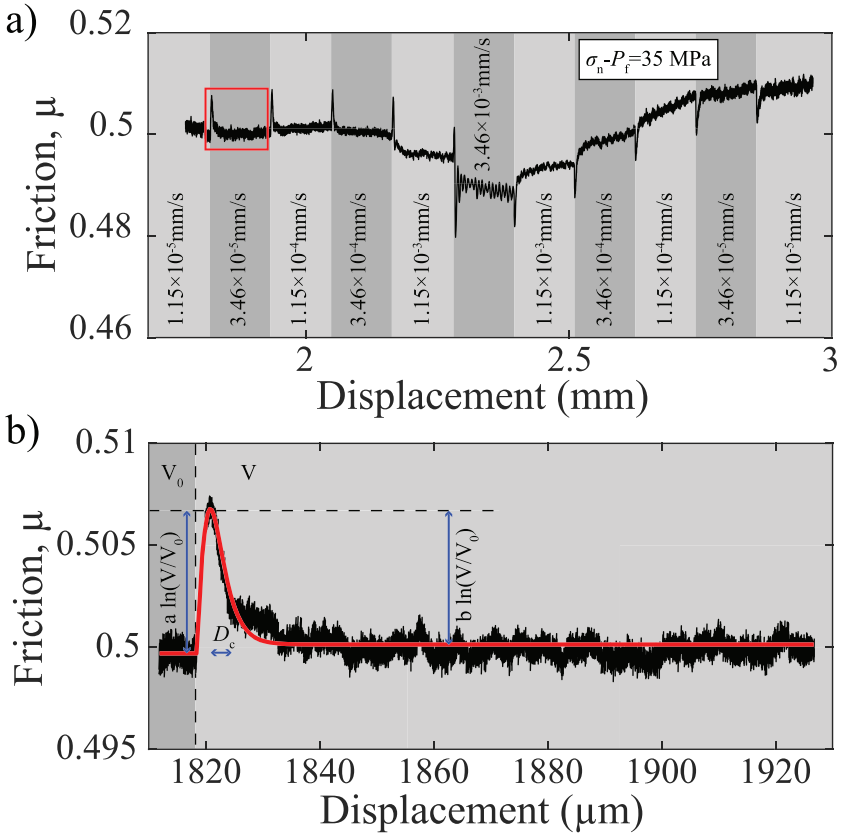

Figure 5. (a) Friction as a function of the displacement along the fault plane for the velocity steps experiment performed at $\sigma_n - P_f = 35$ MPa. (b) Zoom on a velocity step. The experimental curve is presented in black, and the model inversion using the Skarbek and Savage (2019) software is presented in red.

experiments, L_c could not be directly inferred from experimental measurements. However, using the rate-and-state framework, K_c can be estimated (see equation 3).

Note that, even if it has been shown that the effective normal stress acting on the fault has an effect on the stability of the system (e.g., Chambon & Rudnicki, 2001; Dieterich & Linker, 1992; He et al., 1998; He & Wong, 2014; Leeman et al., 2016, 2018), here, no significant difference was found for the effective normal

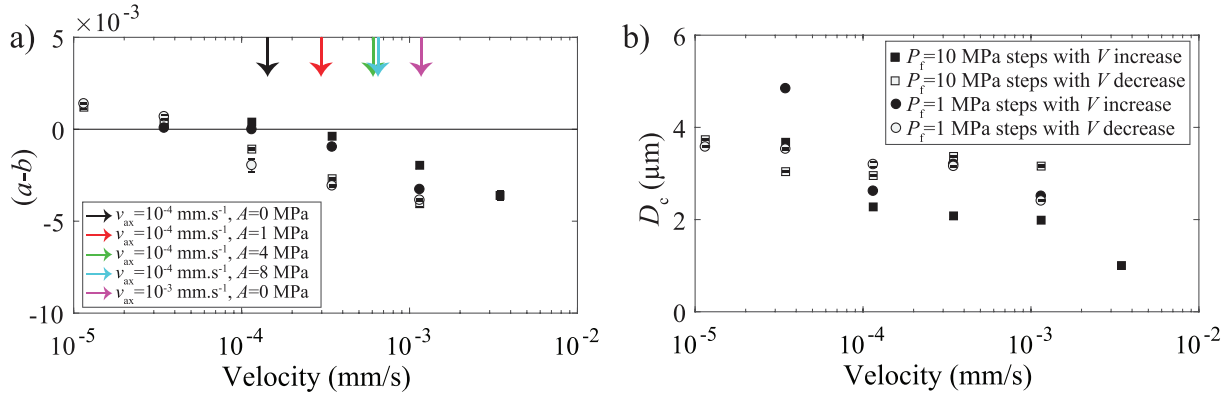

Figure 6. Rate-and-state parameters obtained from the inversion of the experimental data. (a) Displays $(a - b)$ and (b) critical slip distance as a function of velocity. For the experiment conducted at $P_f = 1$ MPa, the inversion was not possible at the velocity of 3.46×10^{-3} mm s^{-1} because stick-slip occurred (i.e., $(a - b) < 0$). The maximum displacement rate of the fault before any instability ($\dot{\delta}_{max}$) is presented with the colored arrows for experiments performed at $P_c = 30$ MPa.

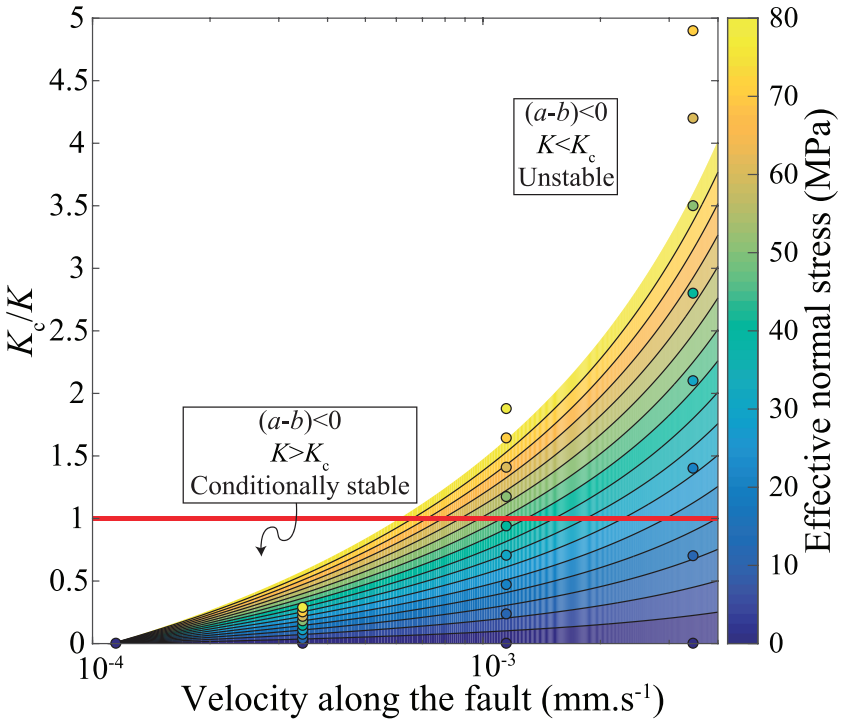

Figure 7. Critical stiffness (K_c) normalized by the stiffness of the experimental surrounding system (K) as a function of the slip velocity. The color bar shows the effective normal stress acting on the fault. The contour plot represents K_c modeled using equation (3). The circles represent K_c/K using the rate-and-state parameters found experimentally. The conditionally stable and unstable domains are separated by the solid red line. The parameters used for the model were obtained from the fit of the parameters experimentally obtained in Figure 6. They are: $(a-b) = -8.97 \times 10^{-4}\ln(V) - 8.2 \times 10^{-3}$, and $D_c = -4.9 \times 10^{-1}\ln(V) - 1.7$. The stiffness of the system (apparatus and Fontainebleau sandstone) was measured to be 62.9 MPa mm^{-1}.

stress tested. Therefore, a, b, and D_c are taken to be independent of the effective normal stress. Using our experimental dataset, K_c can be estimated directly from the rate-and-state parameters found (equation 3). We computed K_c normalized by the system stiffness (K) as function of the sliding velocity (Figure 7). Note that K was measured by deforming an FS sample within the elastic domain while measuring the displacement of the surrounding system (the press column and FS) by the use of an external displacement sensor.

For K_c calculation, we assumed the empirical dependence of the parameters $(a-b)$ and D_c with the sliding velocity (i.e., following the trends in Figure 6). Within the slip rate explored during the fluid pressure oscillating experiments (from 10^{-4} to 10^{-3} mm s^{-1}), the three stability domains are crossed in our experiments (Figure 7). Indeed, we observe a transition between stable and conditionally stable state at a velocity of 1.2×10^{-4} mm s^{-1} and a transition between conditionally stable and unstable at velocity of about 6×10^{-4} mm s^{-1}. The fact that fluid pressure oscillations facilitate stick-slip triggering must originate from the slip rate oscillations in phase with P_f that in turn cause variations of K_c. In summary, the initiation of the AE and stick-slip events is controlled by the coupled rate-and-state and dislocation criterion.

4.4. Implications for Natural and Induced Seismicity

Our experimental results demonstrate that fluid pressure cyclic perturbations in a drained system can lead to fault reactivation and to the onset of the seismicity resulting from slip-rate perturbations. The smaller the confining pressure and the larger the amplitude of the fluid pressure, the larger the seismic triggering potential of the fault in the tested material.

In natural fault systems, it is accepted that a locked velocity weakening (i.e., $(a-b) < 0$) patch on a fault can fail either in a seismic or aseismic manner. If the patch is gently loaded by a creeping surrounding area, and that $K < K_c$, the slip will accelerate to seismic velocity. On the contrary, for conditions where $K > K_c$,

instability cannot nucleate. Our experimental results suggest that if this patch is subjected to fluid pressure oscillations, local variations of slip rate could change the rate-and-state parameters and increase the critical stiffness, allowing for possible seismic slip. Such acceleration of the slip rate can have many fluid-related origins such as oceanic and earth tides (e.g., Houston, 2015; Rubinstein et al., 2008; Rydelek et al., 1992; Scholz et al., 2019), seasonal hydrology (e.g., Bettinelli et al., 2008; Chanard et al., 2014), or fluid production/injection into georeservoir (e.g., Candela et al., 2019; Verdon et al., 2013). In the case of fluid injection, it has been recently suggested that cyclic fluid injections would trigger less seismicity compared to traditional monotonic injections (e.g., Yoon et al., 2014; Zang et al., 2018, 2013). Our experimental results suggest that, under drained conditions, cyclic fluid pressure variations within a faulted reservoir have the effect of varying the slip rate acting on the fault, in turn increasing K_c and promoting unstable slip. However, cyclic fluid injections compared to monotonic fluid injection involve much lower strain rates increases and thus reduce the potentially induced earthquakes. During in situ cyclic fluid injections, fluid pressure tends to homogenize via diffusion processes into the reservoir during period of limited injection. In turn, if the injection frequency increases, this can affect both the drainage conditions and promote high deformation rates. Undrained conditions have been shown to produce local fluid overpressure and favor fault reactivation (Passelègue et al., 2018). Therefore, it is probable that injection frequency, in addition to injection amplitude, might affect fault stability in georeservoirs.

5. Conclusion

We conducted nine triaxial deformation experiments on faulted FS with various fluid pressure oscillation conditions and loading rates. Two additional velocity step experiments were performed in triaxial configurations in order to constrain the rate-and-state parameters of the studied FS. The results show that

1. Faults start to slip when $\mu = 0.52$, in agreement with Byerlee's law.
2. During pore pressure oscillations

a fluid pressure signal controls the instability (i.e., stick-slip and AE events) distribution. In this drained case, instabilities occur mainly at the maximum value of fluid pressure.

b stick-slip events are triggered only after a certain amount of stable sliding. This amount of slip is reduced with increasing P_f oscillation amplitude. We suggest that it is not the pore fluid pressure itself that controls the onset of instability but the variation of slip rate due to the fluid oscillations.

c From the velocity-step experiments, we find that fault stability depends on the slip rate. Increasing the slip velocity promotes unstable slip.

The stability analysis based on the rate-and-state parameters shows that the critical stiffness can be increased with increasing the fault slip rate. We thus infer that the oscillations in slip velocity induced by fluid pressure oscillations can result in critical stiffness changes, in turn promoting the transition from stable to unstable slip and controlling the instability distribution.

Acknowledgments
This work was funded by Gaznat SA (Grant FRICTION: Fault Reactivation during CO_2 sequestraTION). F. X. P. thanks the Swiss National Science Foundation (Grant PZENP2/173613). C. G. thanks the Swiss Federal Office of Energy (EDGAR project). M. V. thanks the ERC project befine (Grant 757290). The authors want to thank Laurent Gastaldo for laboratory assistance. We also thank Barnaby Fryer for proofreading. The authors thank the editor A. Revil, the associate editor Mike Heap, and the reviewers J. W. Rudnicki and Dave Healy for their constructive comments. Raw data can be found at https://zenodo.org/record/3515757#.Xa6vH-gzZaQ or requested from the corresponding author at corentin.noel@epfl.ch.

References

Bettinelli, P., Avouac, J. P., Flouzat, M., Bollinger, L., Ramillien, G., Rajaure, S., & Sapkota, S. (2008). Seasonal variations of seismicity and geodetic strain in the Himalaya induced by surface hydrology. *Earth and Planetary Science Letters*, *266*(3–4), 332–344. https://doi.org/10.1016/j.epsl.2007.11.021

Byerlee, J. (1978). Friction of rocks. In *Rock friction and earthquake prediction*, (pp. 615–626). Basel: Birkhäuser.

Candela, T., Osinga, S., Ampuero, J.-P., Wassing, B., Pluymaekers, M., Fokker, P. A., et al. (2019). Depletion-induced seismicity at the Groningen gas field: Coulomb rate-and-state models including differential compaction effect. *Journal of Geophysical Research: Solid Earth*, *124*(7), 7081–7104. https://doi.org/10.1029/2018JB016670

Chambon, G., & Rudnicki, J. W. (2001). Effects of normal stress variations on frictional stability of a fluid-infiltrated fault. *Journal of Geophisical Research: Solid Earth*, *106*(B6), 11353–11372. https://doi.org/10.1029/2001JB900002

Chanard, K., Avouac, J. P., Ramillien, G., & Genrich, J. (2014). Modeling deformation induced by seasonal variations of continentalwater in the Himalaya region: Sensitivity to Earth elastic structure. *Journal of Geophysical Research: Solid Earth*, *119*, 5097–5113. https://doi.org/10.1002/2013JB010451

Chanard, K., Nicolas, A., Hatano, T., Petrelis, F., Latour, S., Vinciguerra, S., & Schubnel, A. (2019). Sensitivity of acoustic emission triggering to small pore pressure cycling perturbations during brittle creep. *Geophysical Research Letters*, *46*(13), 7414–7423. https://doi.org/10.1029/2019GL082093

Dieterich, J. H. (1978). Time-dependent friction and the mechanics of stick-slip. *Pure and Applied Geophysics*, *116*(4–5), 790–806. https://doi.org/10.1007/BF00876539

Dieterich, J. H. (1979). Modeling of rock friction: 1. Experimental results and constituve equations. *Journal of Geophysical Research*, *84*(9), 2161–2168. https://doi.org/10.1007/BF00876539

Dieterich, J. H., & Linker, M. F. (1992). Fault stability under conditions of variable normal stress. *Geophysical Research Letters*, *19*(16), 1691–1694. https://doi.org/10.1029/92GL01821

Duda, M., & Renner, J. (2013). The weakening effect of water on the brittle failure strength of sandstone. *Geophysical Journal International*, *192*, 1091–1108. https://doi.org/10.1093/gji/ggs090

Ellsworth, W. L. (2013). Injection-induced earthquakes. *Science*, *341*(6142), 1225942. https://doi.org/10.1785/gssrl.83.2.250

Farquharson, J., Heap, M. J., Baud, P., Reuschlé, T., & Varley, N. R. (2016). Pore pressure embrittlement in a volcanic edifice. *Bulletin of Volcanology*, *78*(1), 1–19. https://doi.org/10.1007/s00445-015-0997-9

Fischer, G. J., & Paterson, M. S. (1989). Dilatancy During rock deformation at high temperatures and pressures. *Journal of Geophysical Research*, *94*(B12), 17607–17617. https://doi.org/10.1029/JB094iB12p17607

French, M. E., Zhu, W., & Banker, J. (2016). Fault slip controlled by stress path and fluid pressurization rate. *Geophysical Research Letters*, *43*, 4330–4339. https://doi.org/10.1002/2016GL068893

Gu, J.-C., Rice, J. R., Ruina, A. L., & Tse, S. T. (1984). Stability of quasi-static slip in a single degree of freedom elastic system with rate and state dependent friction. *Journal of the Mechanics and Physics of Solids*, *32*(3), 167–196. https://doi.org/10.1016/s0022-5096(98)00113-6

Guéguen, Y., & Palciauskas, V. (1994). *Introduction to the physics of rocks*. Princeton, NJ: Princeton University Press.

Guérin-Marthe, S., Nielsen, S., Bird, R., Giani, S., & Di Toro, G. (2019). Earthquake nucleation size: Evidence of loading rate dependence in laboratory faults. *Journal of Geophysical Research: Solid Earth*, *124*(1), 689–708. https://doi.org/10.1029/2018JB016803

He, C., Ma, S., & Huang, J. (1998). Transition between stable sliding and stick-slip due to variation in slip rate under variable normal stress condition. *Geophysical Research Letters*, *25*(17), 3235–3238. https://doi.org/10.1029/98GL02518

He, C., & Wong, T. F. (2014). Effect of varying normal stress on stability and dynamic motion of a spring-slider system with rate- and state-dependent friction. *Earthquake Science*, *27*(6), 577–587. https://doi.org/10.1007/s11589-014-0098-4

Heaton, T. H. (1975). Tidal triggering of earthquakes in Iwo-jima island. *Geophysical Journal International*, *43*(2), 307–326. https://doi.org/10.1111/j.1365-246X.1975.tb00637.x

Houston, H. (2015). Low friction and fault weakening revealed by rising sensitivity of tremor to tidal stress. *Nature Geoscience*, *8*(5), 409–415 . https://doi.org/10.1038/ngeo2419

Kanamori, H., & Brodsky, E. E. (2004). The physics of earthquakes. *Reports on Progress in Physics*, *67*(8), 1429–1496. https://doi.org/10.1088/0034-4885/67/8/R03

Kato, N., Yamamoto, K., Yamamoto, H., & Hirasawa, T. (1992). Strain-rate effect on frictional strength and the slip nucleation process. *Tectonophysics*, *211*(1–4), 269–282. https://doi.org/10.1016/0040-1951(92)90064-D

Leeman, J. R., Marone, C., & Saffer, D. M. (2018). Frictional mechanics of slow earthquakes. *Journal of Geophysical Research: Solid Earth*, *123*(9), 7931–7949. https://doi.org/10.1029/2018JB015768

Leeman, J. R., Saffer, D. M., Scuderi, M. M., & Marone, C. (2016). Laboratory observations of slow earthquakes and the spectrum of tectonic fault slip modes. *Nature Communications*, *7*. https://doi.org/10.1038/ncomms11104

Mair, K., & Marone, C. (1999). Friction of simulated fault gouge for a wide range of velocities and normal stresses. *Journal of Geophysical Research*, *104*(B12), 22899–28914. https://doi.org/10.1029/1999JB900279

Marone, C., & Scholz, C. H. (1988). The depth of seismic faulting and the upper transition from stable to unstable slip regimes. *Geophysical Research Letters*, *15*(6), 621–624. https://doi.org/10.1029/GL015i006p00621

Mclaskey, G. C., & Yamashita, F. (2017). Slow and fast ruptures on a laboratory fault controlled by loading characteristics. *Journal of Geophysical Research: Solid Earth*, *122*, 3719–3738. https://doi.org/10.1002/2016JB013681

Michaut, C., Ricard, Y., Bercovici, D., & Sparks, R. S. J. (2013). Eruption cyclicity at silicic volcanoes potentially caused by magmatic gas waves. *Nature Geoscience*, *6*(10), 856–860. https://doi.org/10.1038/ngeo1928

Noël, C., Pimienta, L., & Violay, M. (2019). Time-dependent deformations of sandstone during pore fluid pressure oscillations: Implications for natural and induced seismicity. *Journal of Geophysical Research: Solid Earth*. https://doi.org/10.1029/2018JB016546

Passelègue, F. X., Brantut, N., & Mitchell, T. M. (2018). Fault reactivation by fluid injection: Controls from stress state and injection rate. *Geophysical Research Letters*, *45*(23), 12,837–12,846. https://doi.org/10.1029/2018GL080470

Rice, J. R. (1993). Spatio-temporal complexity of slip on a fault. *Journal of Geophysical Research*, *98*, 9885–9907. https://doi.org/10.1029/93JB00191

Rubinstein, J. L., La Rocca, M., Vidale, J. E., Creager, K. C., & Wech, A. G. (2008). Tidal modulation of nonvolcanic tremor. *Science*, *319*(5860), 186–189. https://doi.org/10.1126/science.1150558

Ruina, A. (1983). Slip instability and state variable friction law. *Journal of Geophysical Research*, *88*, 10359–10370. https://doi.org/10.1029/JB088iB12p10359

Rutqvist, J., Rinaldi, A. P., Cappa, F., Jeanne, P., Mazzoldi, A., Urpi, L., et al. (2016). Fault activation and induced seismicity in geological carbon storage–Lessons learned from recent modeling studies. *Journal of Rock Mechanics and Geotechnical Engineering*, *8*(6), 789–804. https://doi.org/10.1016/j.jrmge.2016.09.001

Rydelek, P. A., & Hass, L. (1994). On estimating the amount of blasts in seismic catalogs with Schuster's method. *Bulletin of the Seismological Society of America*, *84*(4), 1256–1259.

Rydelek, P. A., Sacks, I. S., & Scarpa, R. (1992). On tidal triggering of earthquakes at Campi Flegrei, Italy. *Geophysical Journal International*, *109*(1), 125–135. https://doi.org/10.1111/j.1365-246X.1992.tb00083.x

Scholz, C. H., Tan, Y. J., & Albino, F. (2019). The mechanism of tidal triggering of earthquakes at mid-ocean ridges. *Nature Communications*, *10*(1), 2526. https://doi.org/10.1038/s41467-019-10605-2

Schuster, A. (1897). On lunar and solar periodicities of earthquakes. *Proceedings of the Royal Society of London*, *61*, 455–465. https://doi.org/10.1098/rspl.1897.0060

Scuderi, M. M., Collettini, C., Viti, C., Tinti, E., & Marone, C. (2017). Evolution of shear fabric in granular fault gouge from stable sliding to stick slip and implications for fault slip mode. *Geology*, *45*(8), 731–734. https://doi.org/10.1130/G39033.1

Scuderi, M. M., & Collettini, C. (2018). Fluid injection and the mechanics of frictional stability of shale-bearing faults. *Journal of Geophysical Research: Solid Earth*, *123*(10), 8364–8384. https://doi.org/10.1029/2018JB016084

Skarbek, R. M., & Savage, H. M. (2019). RSFit3000: A MATLAB GUI-based program for determining rate and state frictional parameters from experimental data. *Geosphere*, *15*(5), 1665–1676. https://doi.org/10.1130/GES02122.1

Song, I., & Renner, J. (2008). Hydromechanical properties of Fontainebleau sandstone: Experimental determination and micromechanical modeling. *Journal of Geophysical Research*, *113*, B09211. https://doi.org/10.1029/2007JB005055

Verdon, J. P., Kendall, J.-M., Stork, A. L., Chadwick, R. A., White, D. J., & Bissell, R. C. (2013). Comparison of geomechanical deformation induced by megatonne-scale CO2 storage at Sleipner, Weyburn, and In Salah. *Proceedings of the National Academy of Sciences*, *110*(30), E2762–E2771. https://doi.org/10.1073/pnas.1302156110

Wang, K., & Davis, E. E. (1996). Theory for the propagation of tidally induced pore pressure variations in layered subseafloor formations. *Journal of Geophysical Research*, *101*(B5), 11483–11495. https://doi.org/10.1029/96JB00641

Xu, S., Fukuyama, E., Yamashita, F., Mizoguchi, K., Takizawa, S., & Kawakata, H. (2018). Strain rate effect on fault slip and rupture evolution: Insight from meter-scale rock friction experiments. *Tectonophysics*, *733*, 209–231. https://doi.org/10.1016/j.tecto.2017.11.039

Yoon, J. S., Zang, A., & Stephansson, O. (2014). Numerical investigation on optimized stimulation of intact and naturally fractured deep geothermal reservoirs using hydro-mechanical coupled discrete particles joints model. *Geothermics*, *52*, 165–184. https://doi.org/10.1016/j.geothermics.2014.01.009

Zang, A., Yoon, J. S., Stephansson, O., & Heidbach, O. (2013). Fatigue hydraulic fracturing by cyclic reservoir treatment enhances permeability and reduces induced seismicity. *Geophysical Journal International*, *195*(2), 1282–1287. https://doi.org/10.1093/gji/ggt301

Zang, A., Zimmermann, G., Hofmann, H., Stephansson, O., Min, K.-B., & Kim, K. Y. (2018). How to reduce fluid-injection-induced seismicity. *Rock Mechanics and Rock Engineering.*, *52*(2), 475–493. https://doi.org/10.1007/s00603-018-1467-4

Zhuang, L., Kim, K. Y., Jung, S. G., Diaz, M. B., Min, K.-B., Park, S., et al. (2016). Laboratory study on cyclic hydraulic fracturing of pocheon granite in Korea. In *50th US Rock Mechanics/Geomechanics Symposium. American Rock Mechanics Association*. Houston, Texas, USA: ARMA 16-163.